Accepted Version of the publication: Energy Environ. Sci., 2017,10, 1505-1516. Publication Date: May 19, 2017.
https://doi.org/10.1039/C7EE00977A. © The Royal Society of Chemistry 2017.

MnO_x-decorated carbonized porous silicon nanowire electrodes for high performance supercapacitors†

Sinem Ortaboy,*[abc] John P. Alper,[d] Francesca Rossi,[e] Giovanni Bertoni,[e] Giancarlo Salviati,[e] Carlo Carraro[ab] and Roya Maboudian*[ab]

In this study, manganese oxide (MnO_x)-decorated carbonized porous silicon nanowire arrays (MnO_x/C/PSiNWs) are synthesized through eco-friendly and cost-effective processes. This electrode material system exhibits excellent electrochemical behavior with a specific capacitance reaching 635 F g^{-1}, as well as the highest areal power (100 mWcm^{-2}) and energy (0.46 mW h cm^{-2}) ever reported in a silicon nanowire-based pseudocapacitor electrode. Furthermore, an asymmetric hybrid supercapacitor (AHS) is designed using MnO_x/C/PSiNWs as the positive electrode, carbonized porous silicon nanowires (C/PSiNWs) as the negative electrode and 1-ethyl-3-methyl-imidazolium bis(trifluoromethylsulfonyl)imide (EMIM-TFSI)/acetonitrile as the electrolyte. The supercapacitor shows an excellent power density of 25 kW kg^{-1} and an energy density of 261 W h kg^{-1} at a current density of 0.2 mA cm^{-2} with a large operational potential window (3.6 V) and a good capacitance retention (82% after 10 000 CV cycles). The results show that the MnO_x/C/PSiNW electrodes are promising materials for the future generation of high performance supercapacitors.

Broader context

Electrochemical energy storage (EES) devices have attracted considerable interest due to the increasing demand for high energy and power densities for potential applications in many fields such as portable electronics, sensors, memory back-up systems and implantable medical devices. Supercapacitors are one of the most important classes of EES devices, which deliver higher power than conventional batteries while storing more energy than dielectric capacitors. Recently, extensive research has been focused on developing new advanced materials which are structurally robust and electrically conductive with a large surface area for enhanced charge storage capacity, and are environmentally friendly with low cost. In this study, MnO_x decorated carbonized porous silicon nanowire arrays are produced for the first time and investigated as an electrode material for supercapacitor applications. The highest energy and power densities ever reported in silicon-based pseudo-capacitor electrodes are obtained showing excellent electrochemical performances. An asymmetric hybrid supercapacitor is also produced, showing that this device effectively bridges the gap between conventional batteries and high-power supercapacitors.

[a] *Department of Chemical and Biomolecular Engineering, University of California, Berkeley, California 94720, USA. E-mail: maboudia@berkeley.edu, sinemortaboy@berkeley.edu*
[b] *Berkeley Sensor & Actuator Center, University of California, Berkeley, California 94720, USA*
[c] *Chemistry Department of Engineering Faculty, Istanbul University, Istanbul, 34320, Turkey*
[d] *Nanosciences et Innovation pour les Matériaux, la Biomédecine et l'Énergie, L'Institut Rayonnement-Matière de Saclay (IRAMIS), Commissariat à l'Energie Atomique et aux Energies Alternatives (CEA), Université Paris-Saclay, CEA Saclay, 91191 Gif sur Yvette, France*
[e] *IMEM-CNR Institute, Parco Area delle Scienze 37/A, 43124 Parma, Italy*
† Electronic supplementary information (ESI) available. See DOI: 10.1039/c7ee00977a

Introduction

Supercapacitors are attractive energy storage devices due to their robust lifetimes, rapid charging capabilities and high specific-power capacities for various applications including in mobile and remote sensing platforms, consumer electronics, energy harvesting systems and hybrid electric vehicles.[1–4] These promising energy storage devices store more energy than conventional dielectric capacitors and deliver higher power with longer cycle life than the available battery technologies.[5] Recent studies in the field of supercapacitors have been focused on the use of hybrid materials to further improve the energy density *via* the introduction of transition metal oxides and conductive polymers, which have pseudocapacitive properties.[6,7]

The transition metal oxides, in particular MnO_x, have attracted interest in energy storage applications, because of

their low cost,[8] natural abundance,[9] environmental compatibility and excellent pseudocapacitive properties ($\sim$1370 F g^{-1}).[10] However, their poor electrical conductivity (about 10^{-7}–10^{-8} S cm^{-1}) remains one of the major challenges to be addressed.[11] This drawback can be overcome by depositing thin films of these materials on highly conductive surfaces.

Among many other alternatives, silicon-based materials are favorable for applications in energy conversion and storage devices due to not only their excellent mechanical, electronic, and thermal properties but also their low cost, lack of toxicity and well-established fabrication processes.[12–16] Hu *et al.*[17] demonstrated continuous flow production of SiNWs *via* a metal-assisted chemical etching process for industrial-scale applications.

It is well known that the active surface area is one of the most important factors for improving the performance of supercapacitors because the energy storage is directly proportional to the area of contact between the electrode and the electrolyte.[18] Hochbaum *et al.*[19] reported that porous silicon nanowires (PSiNWs) synthesized by metal-assisted chemical etching (MACE) of silicon have a high specific surface area of $\sim$342 m^2 g^{-1} while non-porous silicon nanowires possess a much lower specific surface area of $\sim$24 m^2 g^{-1}. Furthermore, since the nanowires are synthesized by etching into silicon, they are in direct electrical contact with the underlying substrate which acts as the current collector, hence avoiding the contact-resistance limitations associated with other forms of nanostructured silicon such as Si nanoparticles.[20] Thus, porous silicon nanowires with their high surface area and direct contact to the current collector are promising candidates as supercapacitor electrodes. However, silicon nanowires oxidize readily in an aqueous electrolyte; thus their applications are limited to non-aqueous electrolytes or require surface passivation.[21] In the latter case, we have previously demonstrated that the deposition of an ultrathin layer of graphitic carbon on PSiNWs effectively passivates the PSiNWs while maintaining their high surface area and enhancing their electrical conductivity.[15]

For maximum benefits, it is desirable to combine the advantages of porous Si nanowires for high surface area, carbon coating for chemical stability and high electrical conductivity, and MnO_x for pseudocapacitive behavior and enhanced energy storage. Here, we report the synthesis and characterization of MnO_x-coated carbonized porous silicon nanowires for high-performance supercapacitor electrode materials. The exceptional performance of a supercapacitor device based on this hybrid electrode architecture in an organic electrolyte/organic salt is demonstrated for the first time. Porous silicon nanowires are synthesized using a metal-assisted chemical etching process and encapsulated in an ultrathin graphitic carbon sheath using a chemical vapor deposition (CVD) technique previously described.[15] Growth of an ultrathin MnO_x layer on C/PSiNWs is carried out by an electroless deposition (ELD) method. Scheme 1 shows the key steps in the fabrication of the MnO_x/C/PSiNWs hybrid electrode. Scanning electron microscopy (SEM), high resolution transmission electron microscopy (HR-TEM), X-ray photoelectron spectroscopy (XPS), and Raman spectroscopy are performed to characterize the hybrid electrode. The energy and power density characteristics and the cyclability of the MnO_x/C/PSiNWs electrodes are investigated by cyclic voltammetry and galvanostatic charge/discharge techniques. All the electrochemical measurements are conducted in an EMIM-TFSI ionic liquid electrolyte. Electrochemical measurements reveal that MnO_x/C/PSiNW electrodes yield significant improvements over the previously reported C/PSiNWs in terms of energy density and cycling performance.[15] The enhanced capacitance is attributed to the excellent pseudocapacitive behavior of the MnO_x when coupled to the C/PSiNW nanomaterial.

Results and discussion

Structural and chemical characterization

Representative SEM images of the PSiNWs and MnO_x/C/PSiNWs are shown in Fig. 1a and b, respectively, indicating that the nanowires have retained their uniform, dense and vertically aligned structure through the carbonization and MnO_x coating processes. During the drying process, the CO_2 critical-point drying technique is used to protect the structure of the nanowires from the surface tension forces which cause substantial deformation or collapse when the liquid environment changes to a gaseous one.[22]

Fig. 1c–e report the representative scanning TEM and high angle annular dark field (STEM-HAADF) images of PSiNWs, C/PSiNWs, and MnO_x/C/PSiNWs, respectively. The results indicate that the nanoscale pore structure of the PSiNWs is preserved in the carbonization step and the subsequent coating with MnO_x, a key factor in realizing the full-energy storage potential of these materials. Fig. 1f–h shows the HRTEM images acquired at the surfaces of PSiNWs, C/PSiNWs and MnO_x/C/PSiNWs, respectively. The PSiNW sample (Fig. 1f) presents the expected crystalline structure of Si, with the $\langle 100 \rangle$ crystallographic direction highlighted in the image, along with nanometer-sized pores. The average diameter and pore size of the nanowires are calculated as 139 $\pm$ 13 nm and 9.5 $\pm$ 0.6 nm, respectively, utilizing the TEM images of ten samples. These values compare well to the results reported by Hochbaum *et al.*,[19] following the same PSiNWs synthesis method and achieving a mean pore diameter of 9.7 nm.

Fig. 1g shows that the carbonization step results in the formation, along the NW length, of an ultra-thin (1–5 nm) amorphous carbon sheath, inside the pores and over the external surfaces. This is further supported by the elemental mapping analyses using TEM energy filtering, showing clear evidence of the carbon coverage (Fig. S1a–c, in ESI†). Raman spectroscopy provides additional information about the nature of the carbon coating (Fig. S1d, ESI†). Both the G peak position (1595–1596 cm^{-1}) and the D to G peak intensity ratios (1.34–1.42) indicate a mainly sp^2 hybridized carbon film, consistent with a previous report.[15] This ultra-thin carbon film improves the conductivity as it uniformly coats the entire surface of the nanowires.

After the final MnO_x decoration step, a thicker amorphous layer covering the pores and the outer surfaces is observed by

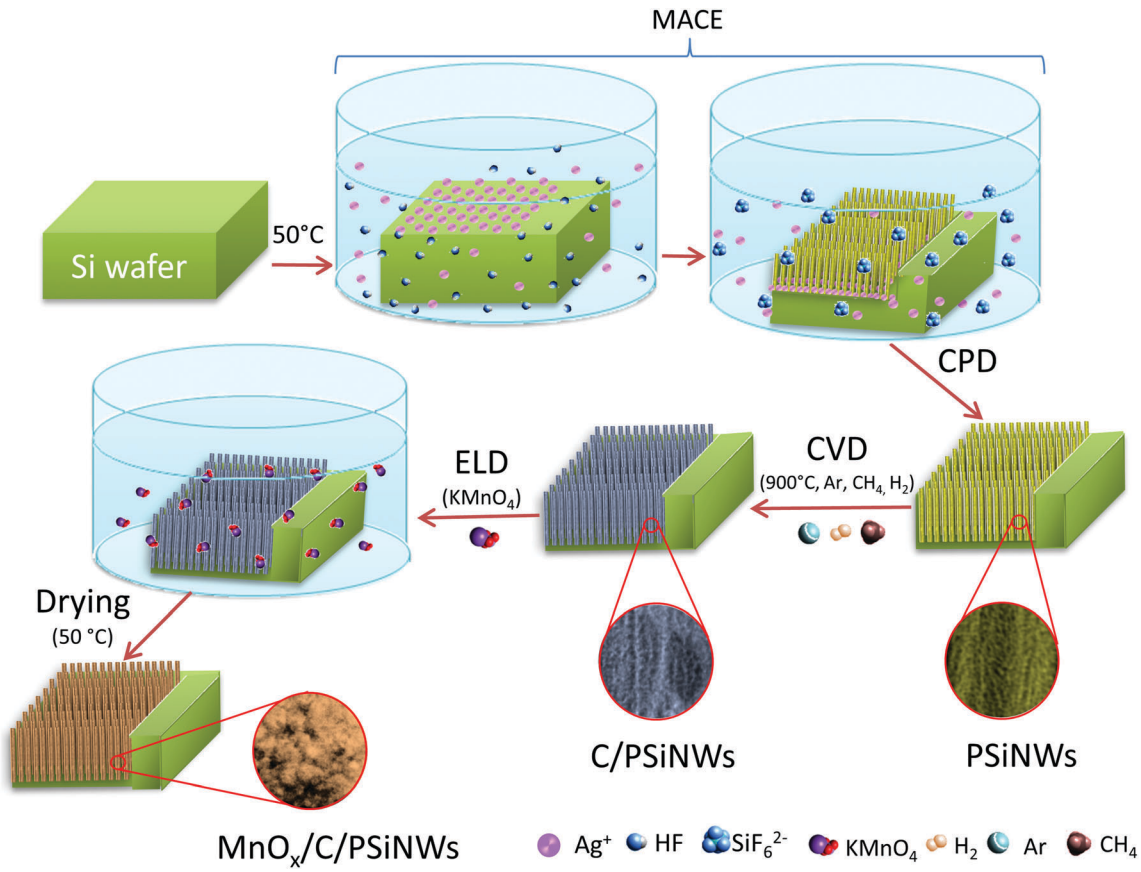

Scheme 1 Schematic illustration of the fabrication processes for the C/PSiNW and MnO_x/C/PSiNW electrodes.

HRTEM (Fig. 1h). The energy-dispersive X-ray (EDX) elemental mapping of the MnO_x/C/PSiNWs electrodes (Fig. 2a) further confirms the deposition of the manganese oxide species on the nanowires. To further elucidate the nature of the deposited MnO_x layer, the electron energy loss spectrum (EELS) from the Mn-$L_{2,3}$ edge obtained on the MnO_x/C/PSiNW sample is shown in Fig. 2b. The spectrum, after background subtraction and multiple scattering deconvolutions, is fitted with a Hartree–Slater cross section taking into account the continuum excitations. The Mn oxidation state is then calculated from the ratio of the shaded areas in the spectrum (L_3 to L_2 peaks) and is found to be 3.3, according to the work of Tan *et al.*[23] The electron energy loss spectra from the Si-L and C-K edges (Fig. 2c), obtained on the nanowires before and after MnO_x deposition and normalized to their integrated areas for comparison,[23] show carbon depletion as a consequence of MnO_x deposition. The deposition process may involve carbon serving as a reducing agent and electron transfer from carbon to MnO_4^-, initiating the heterogeneous nucleation of MnO_x on the active surface. The formation of MnO_x is thus closely related to the carbon structure, with the increasing thickness of the MnO_x film causing gradual consumption of the carbon sheath[24] as suggested by the EELS analysis.

The atomic structures and bonding behavior of the samples are further investigated from X-ray photoelectron spectroscopy. Fig. 3a shows the XPS survey spectra of the C/PSiNWs and the MnO_x/C/PSiNWs. The Si 2p, C 1s, and O 1s peaks are clearly observed in both the spectra, while the spectrum from the MnO_x/C/PSiNWs sample shows the additional Mn 2p peaks, confirming the formation of the Mn-containing species on the surface after the deposition process. The Mn 2p region of the spectrum (Fig. 3b) shows two distinct peaks at 642.5 and 654.1 eV, which correspond to the binding energies of Mn $2p_{3/2}$ and Mn $2p_{1/2}$, respectively. Each peak is deconvoluted into two components with binding energy values of 642.2, 643.7, 653.7 and 654.9 eV, as can be seen in the figure. These binding energy values are attributed to Mn^{2+} and Mn^{3+} oxidation states in the Mn $2p_{3/2}$ and Mn $2p_{1/2}$ peaks, respectively.[25] The results reveal that the MnO_x structure consists of both Mn_2O_3 and MnO phases. In addition, the spin–orbit energy separation between Mn $2p_{3/2}$ and Mn $2p_{1/2}$ peaks is found to be 11.6 eV, which further confirms the presence of a mixed structure of MnO and Mn_2O_3. The ratio of Mn^{3+}/Mn^{2+} under the corresponding XPS peaks is calculated as 0.6, indicating the predominance of the MnO phase over the Mn_2O_3 phase in the MnO_x coating layer. For completeness, the Si 2p, C 1s and O 1s core level spectra obtained on both MnO_x/C/PSiNW and C/PSiNW electrodes are presented in Fig. S2 (ESI†). XPS fitting parameters for deconvolution of the Si 2p, O 1s, Mn 2p and C 1s peaks of the C/PSiNW and MnO_x/C/PSiNW electrodes are also provided in Table S1 (ESI†).

The results presented in this section confirm that a uniform and ultrathin carbon film is obtained on the PSiNW surfaces

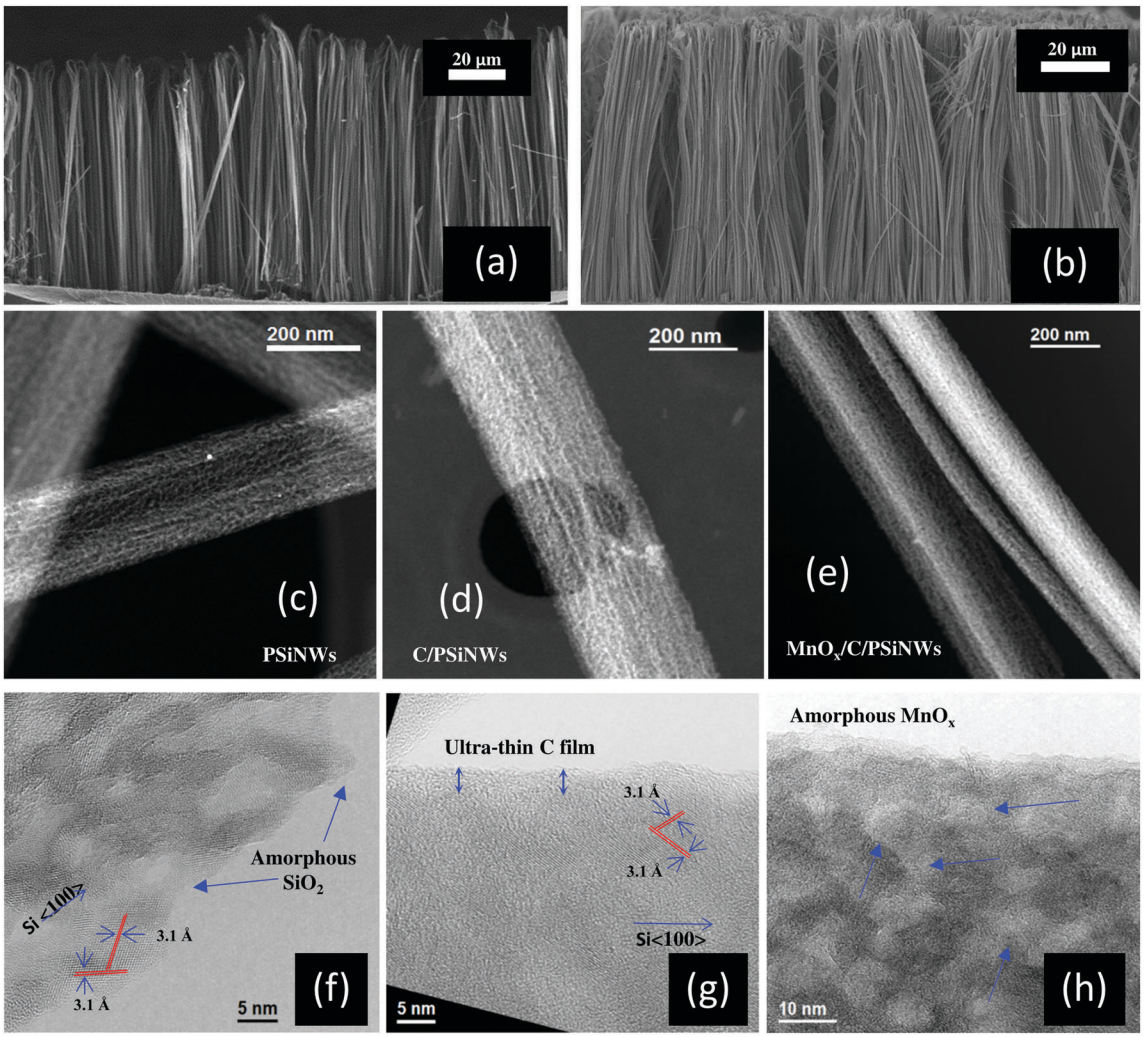

Fig. 1 SEM images of (a) PSiNWs and (b) MnO_x/C/PSiNWs. STEM-HAADF images of (c) PSiNWs, (d) C/PSiNWs, and (e) MnO_x/C/PSiNWs. HR-TEM images of (f) PSiNWs, (g) C/PSiNWs and (h) MnO_x/C/PSiNWs. All the nanowire samples are prepared for 180 min. MACE process at 50 °C. The C/PSiNWs samples are obtained after the carbonization process for 30 min. The MnO_x coating of C/PSiNWs uses 80 mM aqueous $KMnO_4$ solution and a deposition time of 45 min.

after the carbonization process and are consistent with our previous report.[15] The prepared electrode, C/PSiNWs, is successfully coated with MnO_x using an electroless deposition technique, which has several important advantages compared to other film producing techniques, such as low cost, low environmental impact, controllable film thickness, ability to deposit on high aspect ratio structures, good adhesion between the deposited films and active surface, and it being facile and rapid.[26,27]

Electrochemical performance of the MnO_x/C/PSiNW electrode

To evaluate the applicability of the MnO_x/C/PSiNW architecture as an active material for supercapacitors, its electrochemical performance is studied with cyclic voltammetry and galvanostatic charge/discharge techniques. All the measurements are conducted in 0.1 M EMIM-TFSI IL electrolyte in acetonitrile. The effects of different silicon nanowire lengths and different concentrations of $KMnO_4$ solution and different deposition times are investigated.

Representative CV voltammograms of the C/PSiNW and MnO_x/C/PSiNW electrodes are presented in Fig. 4a. The capacitance values obtained on C/PSiNWs compare well to our previous reports.[15] This confirms that the complete pore area of the porous nanowires is likely being utilized for charging, based on surface area information provided in ref. 18. Fig. 4a shows that the hybrid structure of the MnO_x/C/PSiNW electrode provides enhanced capacitive performance (about 5.5 times higher) as compared to the C/PSiNW electrode. The CV curve of the MnO_x-coated electrode shows nearly a rectangular shape with the broad reversible redox peaks demonstrating good pseudocapacitive behavior of MnO_x.[28,29]

Representative galvanostatic charge–discharge (GCD) curves obtained on the C/PSiNW and MnO_x/C/PSiNW electrodes are presented in Fig. 4b. As is shown, the IR drop at the initial stage of galvanostatic discharge curves is higher for the C/PSiNWs (0.06 V) than for the MnO_x/C/PSiNW electrode (0.02 V). This sudden potential decrease is attributed to both the inner

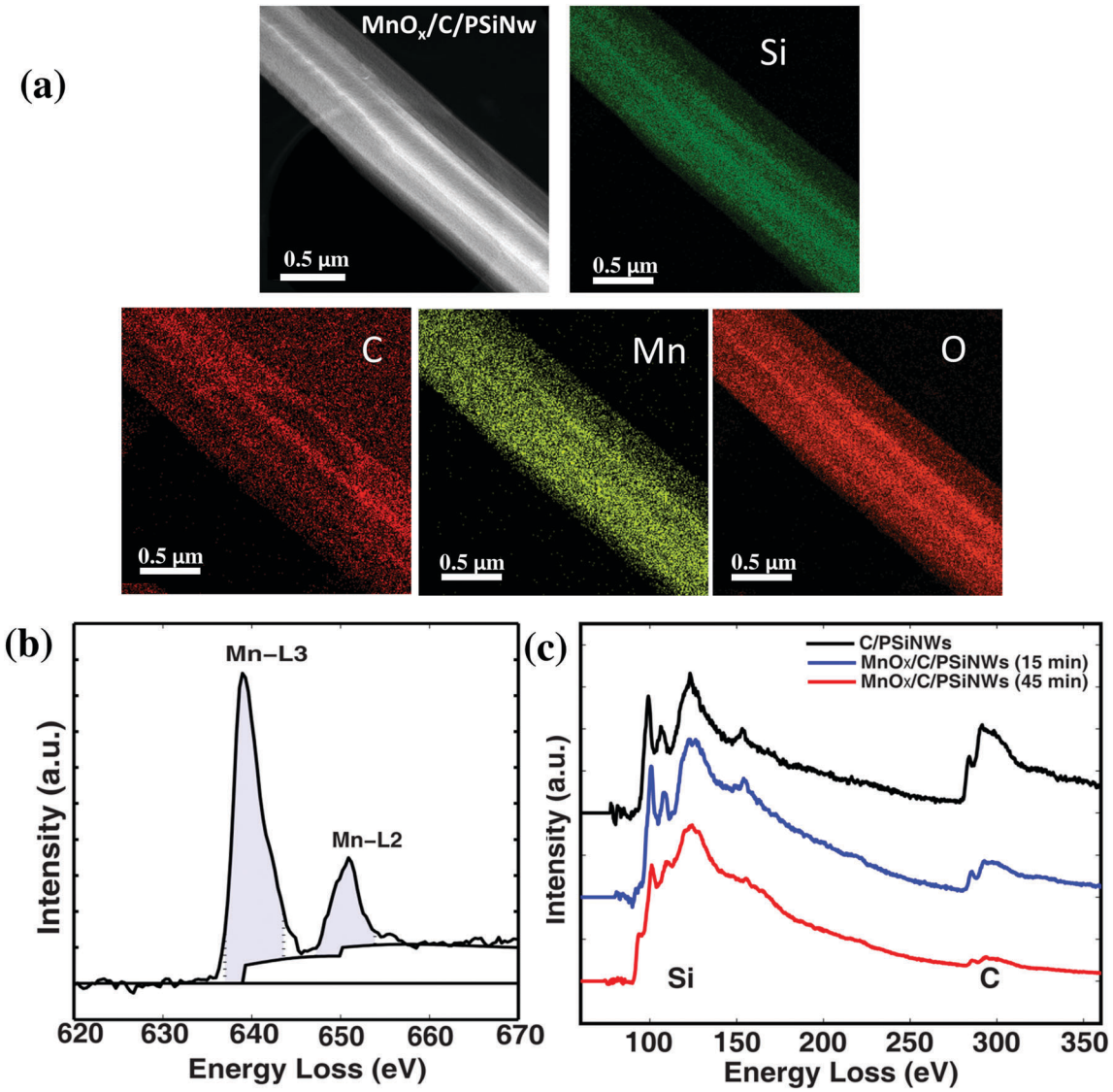

Fig. 2 (a) EDX elemental mapping of the MnO_x/C/PSiNW electrodes, showing elements Si, C, Mn, and O; (b) Mn-$L_{2,3}$ electron energy loss spectrum from MnO_x/C/PSiNWs used to determine the Mn oxidation state. (c) EEL spectra from the Si-L and C-K edges, showing carbon depletion as a consequence of the deposition time in $KMnO_4$ solution. The spectra are normalized to their integrated area for comparison. The electrode synthesis processes are the same as those displayed in Fig. 1.

resistance of the electrode materials and the resistance of the supporting electrolyte.[30] It is also observed that the charge curves have some deviation in the high potential regions due to the presence of the MnO_x layer which enhances the pseudo-capacitive performance. It is well known that a non-ideal triangular shape of the GCD curves is a characteristic of redox reactions occurring in the system.[31] The areal capacitance values of the MnO_x/C/PSiNW and C/PSiNW electrodes as a function of current density are compared in Fig. 4c, again indicating the enhanced capacitance values of the MnO_x/C/PSiNWs irrespective of the current density values.

Fig. 4d shows the effect of the silicon nanowire length on the electrochemical performance (at a current density of 1 mA cm^{-2}) of the MnO_x/C/PSiNW electrodes (for a fixed MnO_x deposition condition of 20 mM $KMnO_4$ concentration and 15 min deposition time). The results indicate that there is a good linear correlation between the nanowire lengths and areal capacitance. Since the nanowire surface area scales linearly with its length, the observed trend confirms that (i) the coating process implemented successfully coats the entirety of the nanowire surface, (ii) the nanowires are electrochemically active and wetted by the electrolyte, and (iii) the ion transport to the nanowire surface does not pose a limitation for the nanowire lengths utilized in this study.

The cycling stability of the MnO_x/C/PSiNW electrode was investigated using CV measurements. Fig. 4e shows the degree of capacitance retention as a function of cycle number at a scan rate of 0.5 V s^{-1} over a potential window of −0.4 to 1.6 V. The MnO_x/C/PSiNW electrode shows excellent cycle stability, with 94% capacitance retention after 5000 cycles and 82% capacitance

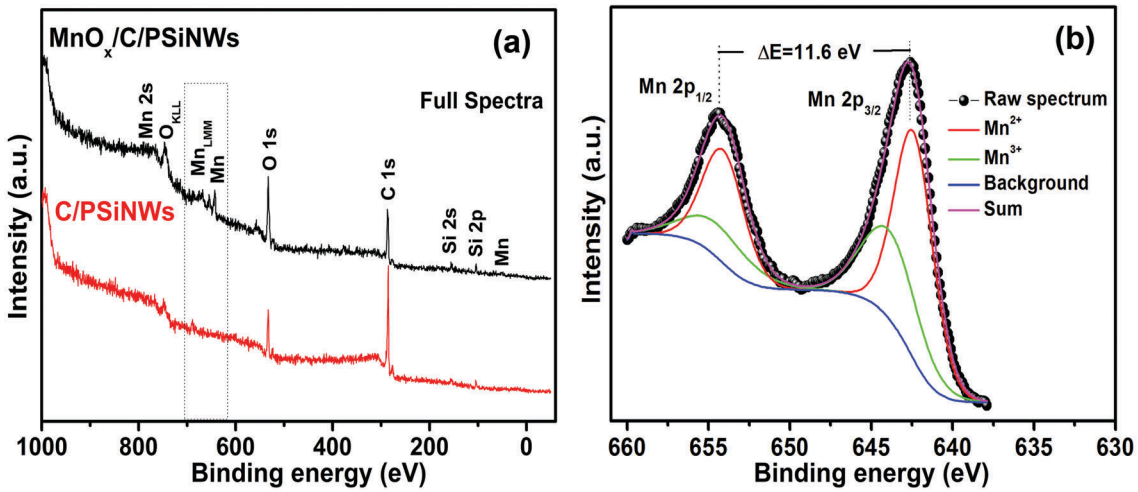

Fig. 3 (a) XPS survey spectra of C/PSiNWs and MnO$_x$/C/PSiNWs, and (b) the Mn 2p region of the X-ray photoelectron spectrum obtained on MnO$_x$/C/PSiNW electrodes. The electrode synthesis process is the same as that displayed in Fig. 1.

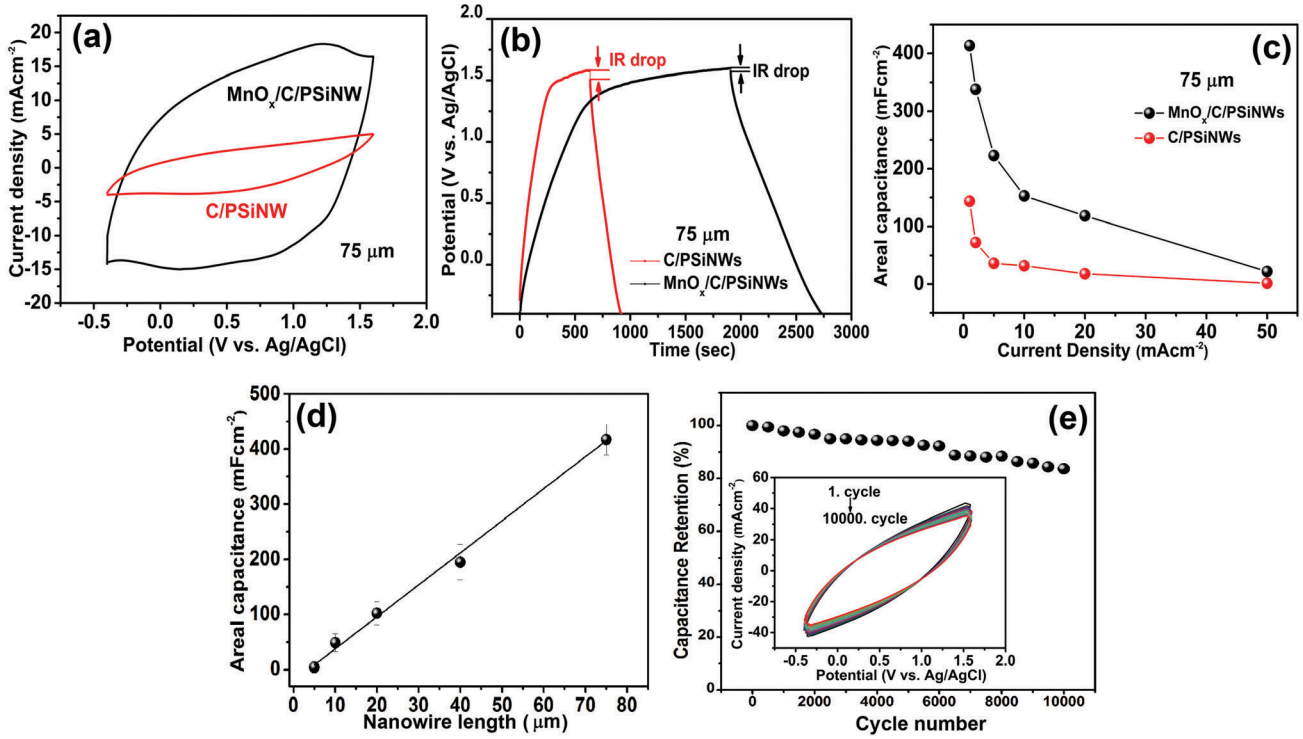

Fig. 4 Comparison of the electrochemical performance of MnO$_x$/C/PSiNW and C/PSiNW electrodes in 0.1 M EMIM-TFSI ionic liquid: (a) cyclic voltammetry curves at a scan rate of 0.1 V s^{-1}, and (b) galvanostatic charge/discharge curves at a current density of 0.1 mA cm^{-2}, showing the effect of the MnO$_x$ coating on the nanowires, (c) variation of areal capacitance *versus* current densities obtained from GCD curves, (d) variation of areal capacitance with the nanowire lengths for MnO$_x$/C/PSiNW electrodes obtained from the GCD curves at a current density of 1 mA cm^{-2}; (e) capacitance retention *versus* cycle number and the corresponding CV curves during 10 000 cycles at a scan rate of 0.5 V s^{-1}. MnO$_x$/C/PSiNW electrodes are prepared using 75 μm nanowire lengths and MnO$_x$ deposition for 15 min from 20 mM KMnO$_4$ solution.

retention after 10 000 cycles. The results show that a significant improvement is obtained as compared to the previously reported C/PSiNW electrodes,[15] which yielded a capacitance retention of ~83% after 5000 GCD cycles. The decrease in capacitance after extended cycling may be due to electrochemical dissolution of the MnO$_x$ layer, as observed in previous studies.[32]

The effects of KMnO$_4$ concentration (ranging from 20 to 100 mM) and bath deposition time (ranging from 5 to 60 min) on the electrochemical performance of the MnO$_x$/C/PSiNW electrode are also investigated. Fig. S3a (ESI†) shows that there is a monotonic increase in capacitance values with increasing KMnO$_4$ concentration due to an increased amount of MnO$_x$ deposited.

The trend continues until the concentration reaches 80 mM, above which a significant decrease is observed. This behavior can be explained by the following: (i) a greater MnO_x concentration leads to a decrease in the nanopore size or causes clogging of active nanopores on the nanowire surface, (ii) the carbon matrix is consumed at the expense of MnO_x deposition (as discussed earlier regarding Fig. 2c) and this phenomenon causes a reduction in electronic conductivity. A similar trend is observed as a function of deposition time (ESI,† Fig. S3b), which may be explained following the same arguments for the effect of $KMnO_4$ concentration. As can be seen from Fig. S3b (ESI†), the maximum capacitance is achieved after 45 min of deposition.

The electrochemical analyses provided above indicate that the best performance is obtained on nanowires with 75 μm lengths and in 80 mM $KMnO_4$ solution for a deposition time of 45 min. In line with these observations, new active electrode materials are prepared under these conditions in order to assess the values of maximum energy and power density. The variation in areal capacitance *versus* current density obtained under these synthesis parameters is presented in Fig. 5a. In order to determine the stable potential window, cyclic voltammograms are examined at different potential windows at a scan rate of 0.1 V s^{-1} (Fig. 5b). From the figure, it is observed that the stable potential window is about 3.1 V (from −1.5 to 1.6 V) and there are weak and broad peaks both in the anodic and the cathodic parts of the curves, indicating pseudocapacitive behavior resulting from Faradaic reactions at the electrode/electrolyte interfaces.[33]

A large operational potential window is one of the key parameters to enhance the performance of a supercapacitor since the energy and power density are related to the square of operational voltage (eqn (3)). The capacitance value of the MnO_x/C/PSiNWs electrode prepared under optimum conditions is determined to be 381 mF cm^{-2} (51 F cm^{-3}, 635 F g^{-1}), even at a current density of 12.5 mA cm^{-2} (1.67 A cm^{-3}, 20 A g^{-1}). As a function of current density from 12.5 to 100 mA cm^{-2}, the maximum areal energy density is calculated as 0.46 mW h cm^{-2} (corresponding to 61 mW h cm^{-3}, 848 W h kg^{-1}) at a power density of 18 mW cm^{-2} (corresponding to 2.5 W cm^{-3}, 34 kW kg^{-1}). The maximum areal power density value is determined to be 100 mW cm^{-2} (corresponding to 13 W cm^{-3}, 167 kW kg^{-1}) at an energy density of 0.13 mW h cm^{-2} (corresponding to 18 mW h cm^{-3}, 93 W h kg^{-1}),

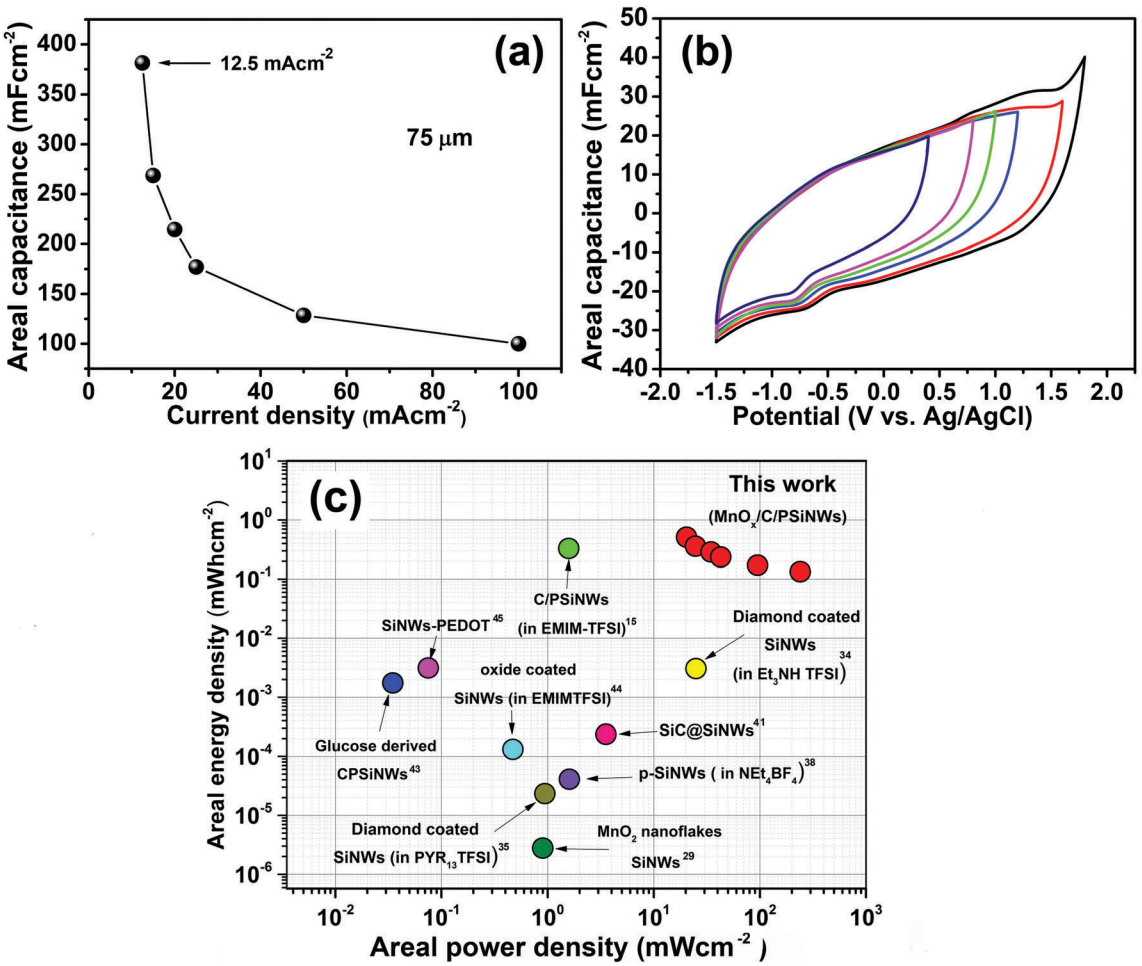

Fig. 5 (a) Areal capacitance *vs.* current density and (b) the corresponding CV voltammograms of MnO_x/C/PSiNW electrodes for different potential windows at a scan rate of 0.1 V s^{-1}, (c) Ragone plot of the MnO_x/C/PSiNW electrodes based on areal power and energy densities. MnO_x/C/PSiNW electrodes are prepared using 75 μm long nanowires, and the MnO_x coating process at a deposition time of 45 min in 80 mM $KMnO_4$ solution.

as shown in Fig. 5c. To the best of our knowledge, these are the highest energy and power densities ever obtained for Si nanowire based supercapacitor electrode materials.[14,15,21,29,34–45] For the uncoated C/PSiNWs, based on our previous work, the maximum volumetric energy density is ~11 mW h cm^{-3} at a power density of ~1.2 W cm^{-3}, and a capacitance retention of 83% is observed after 5000 continuous charge–discharge cycles. In comparison, our present study shows significant improvements in energy density, power density and cycling performance. Some of the recent studies on the electrochemical performance of silicon-based electrodes are also summarized in Table S2 (ESI†).

In addition, this hybrid electrode architecture provides an excellent performance amongst several previous studies based on MnO_x and carbon nanostructured electrode materials such as a C@MnO_2 core shell material (193 F g^{-1} at 0.2 A g^{-1}),[46] a graphene/MnO_2 composite (319 F g^{-1} at 0.2 A g^{-1}),[47] a Mn_3O_4 nanocrystalline/graphene hybrid (517 F g^{-1} at 1 A g^{-1}),[48] a hollowed-out tubular carbon@MnO_2 composite (321 F g^{-1} at 0.5 A g^{-1}),[49] MnO_2 nanoflakes/porous carbon nanofibers (520 F g^{-1} at 0.5 A g^{-1}),[50] reduced coal-derived graphene oxide/Mn_3O_4 (260 F g^{-1} at 50 mA g^{-1}),[51] MnO_2/PANI/GO ternary hybrid composite (512 F g^{-1} at 0.25 A g^{-1})[52] electrode materials, Mn_2O_3/carbon aerogel microbead composites (368 F g^{-1} at 1 A g^{-1}),[53] and nitrogen/manganese oxides co-doped nanoporous carbon materials (564.5 at 0.5 A g^{-1}).[54]

Electrochemical performance of MnO_x/C/PSiNWs//C/PSiNWs hybrid asymmetric supercapacitor

An asymmetric pseudocapacitor device is fabricated using MnO_x/C/PSiNWs and C/PSiNWs electrodes in order to investigate the practical electrochemical performance of these materials. A schematic illustration of the fabricated asymmetric supercapacitor device and an optical image of the device are presented in Fig. 6a and b, respectively. The AHS device with an area of 0.7 cm^{-2} is used to power red (2.2 V), green (3.2 V) and blue (3.3 V) light-emitting diodes (LEDs).

An EIS experiment was performed to better understand the electrochemical behavior and the electrode kinetics. Fig. S4a (ESI†) shows Nyquist plots of an AHS in 2.0 M EMIM-TFSI electrolyte at a frequency ranging between 10 mHz and 100 kHz at open-circuit potential (OCP) with an AC amplitude of 10 mV. The inset in this figure shows the enlarged high frequency region (50–120 Ω). The spectrum shows a single semicircular arc in the high frequency region (inset) and a straight line in the low frequency domain. The extrapolated intercept of the

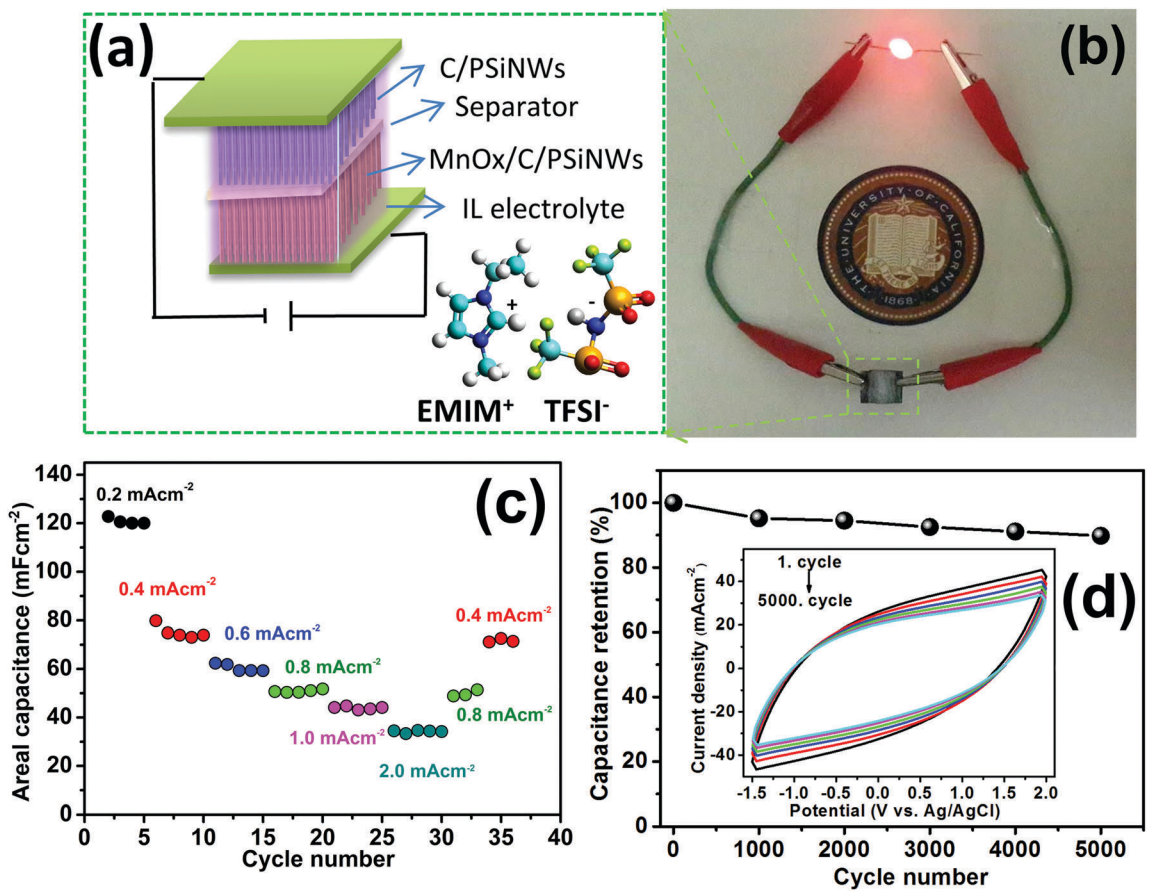

Fig. 6 Asymmetric hybrid supercapacitor device: (a) Schematic illustration, consisting of the MnO_x/C/PSiNW positive electrode, an ionic liquid electrolyte, a separator and the C/PSiNW negative electrode, (b) red light-emitting diode (LED) powered by the fabricated device, (c) rate performance test, and (d) cyclic stability of the device as a function of cycle number; inset shows the corresponding CV curves at a scan rate of 0.1 V s^{-1} for 5000 cycles.

linear portion on the real axis (Z') of the Nyquist plot represents the equivalent series resistance (ESR), which is one of the key parameters to affect the energy storage capability of the supercapacitors, and consists of ionic resistance of an electrolyte and internal resistance of electrodes.[55] The ESR value is determined as 58 Ω. This result is comparable with the previous studies in which ionic liquids are used as a supporting electrolyte.[55,56] The diameter of the semicircular arcs located at the middle section of the Z' axis indicates the charge transfer resistance (R_{ct}) of the supercapacitor. This value is calculated as 23 Ω. Furthermore, the straight line observed at the low frequency region indicates that a rapid ion diffusion pathway dominates the charge storage capability of the AHS.

To demonstrate the rate performance of the AHS device, Fig. 6c shows the areal capacitance for varied values of current density. Representative galvanostatic charge–discharge curves and CV voltammograms can be found in Fig. S4b and c (ESI†). When the current density is decreased from 2.0 to 0.8 and 0.4 mA cm^{-2}, the areal capacitance values recover to the values of 49 mF cm^{-2} (92% retention) and 71 mF cm^{-2} (98% retention), respectively (Fig. 6c). According to the results, it can clearly be said that the cyclic stability test shows high recovery.

Long cycle life stability is one of the most important factors that affect the supercapacitor performance. To evaluate the long-term stability of the device, CV and GCD experiments are performed successively. Initially, 5000 successive CV cycles are applied at a scan rate of 0.5 V s^{-1} in the potential range from −1.5 V to 2.0 V. The results show that the AHS device retained over ∼84% of the original capacitance after 5000 CV cycles (Fig. 6d). The AHS device is also cycled for 3000 consecutive GCD cycles at a current density of 4.0 mA cm^{-2} (Fig. S4d), with a capacitance retention of ∼82% after 3000 cycles.

The volumetric and the specific capacitance values of the AHS device are calculated on the basis of the mass of the active nanowires in the anode and cathode electrode materials. The maximum energy density of the AHS is about 37 mW h cm^{-3} (244 W h kg^{-1}) at a power density of 32 mW cm^{-3} (213 W kg^{-1}) while the maximum power density is about 4 W cm^{-3} (24 kW kg^{-1}) at an energy density of ∼5 mW h cm^{-3} (34 W h kg^{-1}) at a large operational potential window of 3.6 V. Despite the fact that the capacitance is not balanced between the two electrodes, the results show that the AHS device possesses a high performance energy storage ability compared to the recently reported MnO_x, carbon and/or Si based asymmetric supercapacitor devices.[30,57–67] The superior performance of this hybrid architecture can be attributed to the following factors: (i) silicon nanowires with a highly porous structure provide a large active surface; (ii) an ultrathin carbon film deposited on the nanowire arrays provides a highly conductive surface without closing the porous structures; and thus, the active ion diffusion and fast transport process are maintained at all available surfaces; (iii) MnO_x has an ideal pseudocapacitive behavior because its multiple oxidation states provide excellent reversible redox reactions; (iv) the presence of an aprotic ionic liquid (EMIM-TFSI) as an electrolyte in the AHS facilitates redox reactions and increases the operational potential window which is a key parameter to improve the power density of supercapacitor devices.

Conclusions

In summary, an ultra-high performance MnO_x-decorated C/PSiNW supercapacitor electrode material is developed by a cost-effective, simple, and eco-friendly electroless deposition technique. This electrode exhibits very high charge storage capacity with a specific capacitance of 635 F g^{-1}, even at a current density of 20 A g^{-1}, and a specific energy of 848 W h kg^{-1} in 0.1 M EMIM-TFSI ionic liquid electrolyte. These are the highest values ever reported for silicon-based nanowire hybrid electrodes. This electrode system shows a good capacitance retention of 82% after 10 000 CV cycles. The high performance is attributed to the porous nature of the silicon nanowires, the excellent conductivity of the ultra-thin carbon sheath on the porous surface and the outstanding pseudocapacitive properties of the MnO_x layer. Furthermore, an asymmetric hybrid supercapacitor device is fabricated using MnO_x/C/PSiNWs as a positive electrode, C/PSiNWs as a negative electrode and 0.1 M EMIM-TFSI as an electrolyte. A maximum specific power of 24 kW kg^{-1} and a maximum specific energy of 244 W h kg^{-1} are achieved with a high operational potential range of 3.6. These results suggest that the MnO_x/C/PSiNWs architecture is promising for hybrid supercapacitor applications, and they effectively bridge the gap between conventional batteries and high-power supercapacitors.

Experimental details

Fabrication of MnO_x-coated carbonized porous Si nanowires

The synthesis process is schematically shown in Scheme 1. PSiNWs are produced *via* wet etching of highly-doped p-type Si substrates (0.001–0.005 Ω cm) using an oxidant/etchant bath of $AgNO_3$ and HF at the bath temperature of 50 °C. After the synthesis, the residual silver dendrites are removed by dilute HNO_3. Then, the CO_2 supercritical point drying (CPD) process is conducted to prevent the agglomeration of the nanowire arrays. The chemical vapor deposition (CVD) process is carried out to produce carbonized PSiNWs by exposing to a CH_4/Ar atmosphere at 900 °C. For MnO_x coating, a chemical bath deposition technique is performed using aqueous $KMnO_4$ solution. Different concentrations and different deposition times are applied to determine the optimum parameters, as detailed below.

Preparation of porous silicon nanowire arrays

Porous silicon nanowires are prepared in a one-step MACE procedure according to a previously published method.[15] Briefly, a single crystal, ⟨100⟩ oriented, p-type silicon substrate (0.001–0.005 Ω cm, University Wafer Inc., Boston, U.S.A.) is cut into pieces with dimensions of 1.0 cm × 1.0 cm. Prior to etching, the Si coupons are cleaned by ultrasonication in acetone (Merck), isopropyl alcohol (IPA, ≥99.5%, Sigma-Aldrich) and deionized water (DI, 18 MΩ cm), respectively. The UV/ozone (UVO) cleaning process is performed for removing trace amounts of organic contamination. The substrates are also immersed in concentrated hydrofluoric acid (HF, 48%, Merck) for 5 min to eliminate the native oxide from the surface. The back sides of the samples are coated with a thin layer of nylon polymer in order to

prevent the formation of wires on this side during the etching process. In addition, a ~3 mm wide strip at the top of the polished side, which is used for electrical contact with the electrode, is also coated by the nylon polymer resist. The first step of the etching process is carried out in a 5.0 M HF/20 mM $AgNO_3$ (≥99.0%, Aldrich) aqueous solution and for varying times between 20 and 180 min at 50 °C in order to synthesize PSiNWs with different wire lengths. After the etching process, Ag dendrites deposited on the sample surface are removed carefully by peeling and then immersing in deionized (DI) water at least three times. The remaining Ag layer is removed in 3.5 M HNO_3 (65%, Merck) solution. This step is continued until the color of the surface turns to black, at which point the sample is immediately dipped in DI water. Next, the sample is moved to acetone in order to remove the polymer coating from the back surface. The samples are rinsed in anhydrous isopropanol to remove residual water. Dehydration of the samples is performed in 3 consecutive rinse steps. For every step, the samples are kept in an anhydrous isopropanol solution for 15 min. Finally, the dehydrated samples are transferred to the commercial CO_2 supercritical point drying apparatus (CPD, Tousimis AutoSamdri 815 B) and dried to prevent the agglomeration of the nanowire arrays.

Preparation of C/PSiNW and MnO_x/C/PSiNW electrodes

The as-prepared PSiNWs are carbonized *via* a chemical vapor deposition process through the thermal decomposition of methane (CH_4, 99.9%, Praxair) as the carbon precursor (Lindberg Blue/m). The samples are heated to 900 °C (at a rate of 15 °C min^{-1}) under 200 sccm of flowing Ar (99.9%, Praxair). Then, CH_4 is introduced at a flow rate of 4 sccm for 30 min. The carbonized PSiNWs are cooled to room temperature at a rate of 15 °C min^{-1} under Ar.

MnO_x layers are deposited on the C/PSiNWs by means of an electroless deposition method. $KMnO_4$ (≥99%, Fischer Scientific) is used as the precursor for MnO_x deposition. In order to evaluate the optimum deposition parameters, the $KMnO_4$ concentrations are varied between 20 and 100 mM, and the ELD time intervals are varied ranging from 5 to 60 min. After the deposition, the samples are removed from the chemical bath and rinsed several times with DI water; then dried in air. During all ELD processes, the $KMnO_4$ solution is kept at room temperature (20 ± 1 °C).

Fabrication of asymmetric hybrid supercapacitors

Asymmetric hybrid supercapacitors are assembled with the MnO_x/C/PSiNWs as the positive electrode and C/PSiNWs as the negative electrode and using 2.0 M EMIM-TFSI ionic liquid electrolyte. The sandwich-type AHS is constructed by sandwiching a cellulosic filter paper (Whatman, 8 mm) soaked with the EMIM-TFSI electrolyte between the electrodes. The final thickness of the supercapacitor is about 1.5 mm, and the total geometric areas of the active surfaces are 0.7 × 1.0 cm^2.

Characterization techniques and electrochemical measurements

The surface morphologies and microstructures of the electrodes are investigated using field emission scanning electron microscopy (FE-SEM Quanta 3D FEG); the crystalline structure and sample composition are analyzed by transmission electron microscopy (TEM) using a JEOL 2200FS field-emission microscope equipped with an in-column Ω filter. The nanowire samples are sonicated in ethanol and dropped on holey carbon-covered nickel grids for the TEM analysis. The microscope is operated at 200 kV either in TEM mode to perform high resolution imaging and acquire elemental maps by energy-filtering (a three windows method) on the Si-L and C-K edges, or in scanning mode to perform high angle annular dark field imaging and to acquire elemental maps by energy dispersive X-ray (EDX) spectroscopy. Electron energy loss spectra from individual NWs are acquired in TEM mode, using the filter in spectroscopy mode, and making use of a set of apertures to fix the convergence and acceptance semi-angles to 3.0 mrad and 6.2 mrad, respectively.

X-Ray photoelectron spectroscopy is carried out on an Omicron XPS EA 125 with Mg Kα as the X-ray source and the C 1s peak at 284.8 eV is used as an internal standard. The deconvolution of the XPS spectra is performed using Casa XPS Software version 2.3.16, and Gaussian–Lorentzian functions are applied after Shirley background correction for each spectrum.

Electrochemical measurements are performed with a CHI 600 electrochemical workstation. The performance of single electrodes is investigated using a three-electrode system with an Ag/AgCl reference and Pt wire counter electrodes. A two-electrode system is applied for the asymmetric device measurements. Electrochemical experiments are conducted in acetonitrile (ACN) containing 0.1 M and 2.0 M EMIM-TFSI ionic liquids for the electrode and the AHS device, respectively. Galvanostatic charge–discharge (GCD) tests are performed at various current densities. Before conducting the electrochemical experiments, the samples are cycled ten times to remove the adsorbed impurities from the active electrode surface.

The volumetric capacitance is calculated from the GCD curves and the CV curves according to the following equations:[68]

$$C_{CV} = \frac{\int_{V_a}^{V_c} I\,dV}{A\theta(V_c - V_a)} \quad (1)$$

$$C_{GD} = \frac{I\Delta t}{A(V_c - V_a)} \quad (2)$$

where C is the areal capacitance in F cm^{-2}, A (cm^2) is the area of the active electrode surface, θ is the scan rate (V s^{-1}), $\int_{V_a}^{V_c} I\,dV$ is the integrated area under the CV curve, $(V_c - V_a)$ is the potential window (V) and Δt is the discharge time (s).

The energy density (E) and the power density (P) are determined from eqn (3) and (4), respectively:

$$E = \frac{1}{2}C(\Delta V)^2 \quad (3)$$

$$P = \frac{E}{\Delta t} \quad (4)$$

where C is the areal capacitance (mF cm^{-2}), ΔV is the potential window (V), P represents the power density (W h cm^{-2}) and Δt is the discharge time (s).

The mass of the active electrode materials is measured using a microbalance (Sartorius ME415S) with a precision of 0.01 mg.[69–71] Mass values are measured by mechanically removing the nanowires from the Si wafer substrates. The measurements are replicated twice for five samples. According to the results, the mass of MnO_x/C/PSiNWs is calculated to be 0.42 ± 0.04 mg while that of C/PSiNWs is found to be 0.33 ± 0.02 mg based on an electrode area of 0.7 cm^2.

Acknowledgements

This study is supported by the Scientific and Technological Research Council of Turkey (TUBITAK) 2219-International Postdoctoral Research Fellowship Program (App. No: 1059B191401401), the National Science Foundation of the United States, and the Industrial Members of the Berkeley Sensor & Actuator Center. One of the authors (S. O.) also acknowledges the "Istanbul University, Engineering Faculty, Chemistry Department" for additional financial support. The authors sincerely thank Raphael Brechbühler, Yuan Gao and Hu Long for their kind help.

Notes and references

1 L. Sun, X. Wang, K. Zhang, J. Zou and Q. Zhang, *Nano Energy*, 2016, **22**, 11–18.
2 J. R. Miller and P. Simon, *Science*, 2008, **321**, 651–652.
3 T. Chen and L. Dai, *Mater. Today*, 2013, **16**, 272–280.
4 X. Zhang, Z. Zhang, H. Pan, W. Salman, Y. Yuan and Y. Liu, *Energy Convers. Manage.*, 2016, **118**, 287–294.
5 D. S. Achilleos and T. A. Hatton, *J. Colloid Interface Sci.*, 2015, **447**, 282–301.
6 G. A. Snook, P. Kao and A. S. Best, *J. Power Sources*, 2011, **196**, 1–12.
7 V. Augustyn, P. Simon and B. Dunn, *Energy Environ. Sci.*, 2014, **7**, 1597.
8 M. Stanley, Global price of manganese from 2007 to 2018 (in U.S. dollars per dry metric ton unit), https://www.statista.com/statistics/247633/manganese-price-forecast/, accessed 13.03.2017.
9 L. A. Corathers, H. A. Fatah and G. J. Wallace, U.S. Geological Survey, 2016, pp. 1–21, https://minerals.usgs.gov/minerals/pubs/commodity/manganese/myb1-2013-manga.pdf, accessed 13.03.2017.
10 Y. Zhao, W. Ran, J. He, Y. Huang, Z. Liu, W. Liu, Y. Tang, L. Zhang, D. Gao and F. Gao, *Small*, 2015, **11**, 1310–1319.
11 H. Wang, L.-F. Cui, Y. Yang, H. Sanchez Casalongue, J. T. Robinson, Y. Liang, Y. Cui and H. Dai, *J. Am. Chem. Soc.*, 2010, **132**, 13978–13980.
12 C. Liu, J. J. Gallagher, K. K. Sakimoto, E. M. Nichols, C. J. Chang, M. C. Y. Chang and P. Yang, *Nano Lett.*, 2015, **15**, 3634–3639.
13 T. Zhang, S. Wu, J. Xu, R. Zheng and G. Cheng, *Nano Energy*, 2015, **13**, 433–441.
14 D. Aradilla, P. Gentile, G. Bidan, V. Ruiz, P. Gómez-Romero, T. J. S. Schubert, H. Sahin, E. Frackowiak and S. Sadki, *Nano Energy*, 2014, **9**, 273–281.
15 J. P. Alper, S. Wang, F. Rossi, G. Salviati, N. Yiu, C. Carraro and R. Maboudian, *Nano Lett.*, 2014, **14**, 1843–1847.
16 C. K. Chan, H. Peng, G. Liu, K. McIlwrath, X. F. Zhang, R. A. Huggins and Y. Cui, *Nat. Nanotechnol.*, 2008, **3**, 31–35.
17 Y. Hu, K.-Q. Peng, L. Liu, Z. Qiao, X. Huang, X.-L. Wu, X.-M. Meng and S.-T. Lee, *Sci. Rep.*, 2014, **4**, 3667.
18 X. Lang, A. Hirata, T. Fujita and M. Chen, *Nat. Nanotechnol.*, 2011, **6**, 232–236.
19 D. G. Allon, I. Hochbaum, Y. J. Hwang and P. Yang, *Nano Lett.*, 2009, **9**, 3550–3554.
20 M. McGraw, P. Kolla, B. Yao, R. Cook, Q. Quiao, J. Wu and A. Smirnova, *Polymer*, 2016, **99**, 488–495.
21 J. P. Alper, M. Vincent, C. Carraro and R. Maboudian, *Appl. Phys. Lett.*, 2012, **100**, 163901.
22 V. Passi, E. Dubois, A. Lecestre, A. S. Linde, B. D. Bois and J.-P. Raskin, *Microelectron. Eng.*, 2013, **103**, 57–65.
23 H. Tan, J. Verbeeck, A. Abakumov and G. Van Tendeloo, *Ultramicroscopy*, 2012, **116**, 24–33.
24 S.-W. Lee, S.-M. Bak, C.-W. Lee, C. Jaye, D. A. Fischer, B.-K. Kim, X.-Q. Yang, K.-W. Nam and K.-B. Kim, *J. Phys. Chem. C*, 2014, **118**, 2834–2843.
25 N. Li, J.-Y. Wang, Z.-Q. Liu, Y.-P. Guo, D.-Y. Wang, Y.-Z. Su and S. Chen, *RSC Adv.*, 2014, **4**, 17274–17281.
26 A. E. Fischer, M. P. Saunders, K. A. Pettigrew, D. R. Rolison and J. W. Long, *J. Electrochem. Soc.*, 2008, **155**, A246.
27 B. Tao, J. Zhang, F. Miao, S. Hui and L. Wan, *Electrochim. Acta*, 2010, **55**, 5258–5262.
28 C. Xiong, T. Li, A. Dang, T. Zhao, H. Li and H. Lv, *J. Power Sources*, 2016, **306**, 602–610.
29 D. P. Dubal, D. Aradilla, G. Bidan, P. Gentile, T. J. Schubert, J. Wimberg, S. Sadki and P. Gomez-Romero, *Sci. Rep.*, 2015, **5**, 9771.
30 M. Kim and J. Kim, *Phys. Chem. Chem. Phys.*, 2014, **16**, 11323–11336.
31 K. Wang, H. Wu, Y. Meng, Y. Zhang and Z. Wei, *Energy Environ. Sci.*, 2012, **5**, 8384–8389.
32 Z. Wang, Q. Qin, W. Xu, J. Yan and Y. Wu, *ACS Appl. Mater. Interfaces*, 2016, **8**, 18078–18088.
33 C. Choi, S. H. Kim, H. J. Sim, J. A. Lee, A. Y. Choi, Y. T. Kim, X. Lepro, G. M. Spinks, R. H. Baughman and S. J. Kim, *Sci. Rep.*, 2015, **5**, 9387.
34 D. Aradilla, F. Gao, G. Lewes-Malandrakis, W. Müller-Sebert, D. Gaboriau, P. Gentile, B. Iliev, T. Schubert, S. Sadki, G. Bidan and C. E. Nebel, *Electrochem. Commun.*, 2016, **63**, 34–38.
35 F. Gao, G. Lewes-Malandrakis, M. T. Wolfer, W. Müller-Sebert, P. Gentile, D. Aradilla, T. Schubert and C. E. Nebel, *Diamond Relat. Mater.*, 2015, **51**, 1–6.
36 I. Oh, M. Kim and J. Kim, *Chem. Eng. J.*, 2015, **273**, 82–91.
37 R. Huang, X. Fan, W. Shen and J. Zhu, *Appl. Phys. Lett.*, 2009, **95**, 133119.
38 F. Thissandier, A. Le Comte, O. Crosnier, P. Gentile, G. Bidan, E. Hadji, T. Brousse and S. Sadki, *Electrochem. Commun.*, 2012, **25**, 109–111.
39 M. Kim, Y. Yoo and J. Kim, *J. Power Sources*, 2014, **265**, 214–222.

40 C. H. Chang, B. Hsia, J. P. Alper, S. Wang, L. E. Luna, C. Carraro, S. Y. Lu and R. Maboudian, *ACS Appl. Mater. Interfaces*, 2015, **7**, 26658–26665.

41 J. P. Alper, M. S. Kim, M. Vincent, B. Hsia, V. Radmilovic, C. Carraro and R. Maboudian, *J. Power Sources*, 2013, **230**, 298–302.

42 J. P. Alper, A. Gutes, C. Carraro and R. Maboudian, *Nanoscale*, 2013, **5**, 4114–4118.

43 R. R. Devarapalli, S. Szunerits, Y. Coffinier, M. V. Shelke and R. Boukherroub, *ACS Appl. Mater. Interfaces*, 2016, **8**, 4298–4302.

44 N. Berton, M. Brachet, F. Thissandier, J. Le Bideau, P. Gentile, G. Bidan, T. Brousse and S. Sadki, *Electrochem. Commun.*, 2014, **41**, 31–34.

45 D. Aradilla, G. Bidan, P. Gentile, P. Weathers, F. Thissandier, V. Ruiz, P. Gomez-Romero, T. J. S. Schubert, H. Sahin and S. Sadki, *RSC Adv.*, 2014, **4**, 26462–26467.

46 R. Liu, E. Liu, R. Ding, K. Liu, Y. Teng, Z. Luo, Z. Li, T. Hu and T. Liu, *Ceram. Int.*, 2015, **41**, 12734–12741.

47 J. Hao, Y. Zhong, Y. Liao, D. Shu, Z. Kang, X. Zou, C. He and S. Guo, *Electrochim. Acta*, 2015, **167**, 412–420.

48 X. Yang, Y. He, Y. Bai, J. Zhang, L. Kang, H. Xu, F. Shi, Z. Lei and Z.-H. Liu, *Electrochim. Acta*, 2016, **188**, 398–405.

49 B. Mu, W. Zhang, W. Xu and A. Wang, *Electrochim. Acta*, 2015, **178**, 709–720.

50 D. Zhou, H. Lin, F. Zhang, H. Niu, L. Cui, Q. Wang and F. Qu, *Electrochim. Acta*, 2015, **161**, 427–435.

51 F. Gao, J. Qu, Z. Zhao, Q. Zhou, B. Li and J. Qiu, *Carbon*, 2014, **80**, 640–650.

52 G. Han, Y. Liu, L. Zhang, E. Kan, S. Zhang, J. Tang and W. Tang, *Sci. Rep.*, 2014, **4**, 4824.

53 X. Wang, L. Liu, X. Wang, L. Yi, C. Hu and X. Zhang, *Mater. Sci. Eng., B*, 2011, **176**, 1232–1238.

54 Z. J. Zhang, L. X. Cheng and X. Y. Chen, *Electrochim. Acta*, 2015, **161**, 84–94.

55 L. Y. Chen, J. L. Kang, Y. Hou, P. Liu, T. Fujita, A. Hirata and M. W. Chen, *J. Mater. Chem. A*, 2013, **1**, 9202.

56 B. Shen, J. Lang, R. Guo, X. Zhang and X. Yan, *ACS Appl. Mater. Interfaces*, 2015, **7**, 25378–25389.

57 X. She, X. Zhang, J. Liu, L. Li, X. Yu, Z. Huang and S. Shang, *Mater. Res. Bull.*, 2015, **70**, 945–950.

58 J. Chen, Y. Wang, J. Cao, Y. Liu, J.-H. Ouyang, D. Jia and Y. Zhou, *Electrochim. Acta*, 2015, **182**, 861–870.

59 X.-Y. Zhang, L.-Q. Han, S. Sun, C.-Y. Wang and M.-M. Chen, *J. Alloys Compd.*, 2015, **653**, 539–545.

60 R. T. Vinny, K. Chaitra, K. Venkatesh, N. Nagaraju and N. Kathyayini, *J. Power Sources*, 2016, **309**, 212–220.

61 X. Zhang, D. Zhao, Y. Zhao, P. Tang, Y. Shen, C. Xu, H. Li and Y. Xiao, *J. Mater. Chem. A*, 2013, **1**, 3706–3712.

62 Y. Sun, Y. Cheng, K. He, A. Zhou and H. Duan, *RSC Adv.*, 2015, **5**, 10178–10186.

63 Z. Lei, J. Zhang and X. S. Zhao, *J. Mater. Chem.*, 2012, **22**, 153–160.

64 J. Liu, L. Zhang, H. B. Wu, J. Lin, Z. Shen and X. W. Lou, *Energy Environ. Sci.*, 2014, **7**, 3709–3719.

65 P. F. R. Ortega, J. P. C. Trigueiro, G. G. Silva and R. L. Lavall, *Electrochim. Acta*, 2016, **188**, 809–817.

66 P. Yang, X. Xiao, Y. Li, Y. Ding, P. Qiang, X. Tan, W. Mai, Z. Lin, W. Wu, T. Li, H. Jin, P. Liu, J. Zhou, C. P. Wong and Z. L. Wang, *ACS Nano*, 2013, **7**, 2617–2626.

67 C. Xu, Z. Li, C. Yang, P. Zou, B. Xie, Z. Lin, Z. Zhang, B. Li, F. Kang and C.-P. Wong, *Adv. Mater.*, 2016, **28**, 4105–4110.

68 D. Wu, S. Xu, M. Li, C. Zhang, Y. Zhu, Y. Xu, W. Zhang, R. Huang, R. Qi, L. Wang and P. K. Chu, *J. Mater. Chem. A*, 2015, **3**, 16695–16707.

69 H. Chen, Z. Dong, Y. Fu and Y. Yang, *J. Solid State Electrochem.*, 2010, **14**, 1829–1834.

70 J. Benson, S. Boukhalfa, A. Magasinski, A. Kvit and G. Yushin, *ACS Nano*, 2012, **6**, 118–125.

71 D. Aradilla, F. Gao, G. Lewes-Malandrakis, W. Müller-Sebert, P. Gentile, M. Boniface, D. Aldakov, B. Iliev, T. J. S. Schubert, C. E. Nebel and G. Bidan, *ACS Appl. Mater. Interfaces*, 2016, **8**, 18069–18077.